Imaging Velocity Profiles: Flow through an Abrupt Contraction and Expansion

Yang Xia and Paul T. Callaghan
Dept. of Physics and Biophysics, Massey University, Palmerston North, New Zealand

Kenneth R. Jeffrey
Dept. of Physics, University of Guelph, Guelph, Ontario, Canada N1G 2W1

Dynamic nuclear magnetic resonance (NMR) microscopy has been used to study the laminar flow of water through cylindrical tubes in the vicinity of both an abrupt expansion and an abrupt contraction. Radial profiles of the velocity have been obtained, at a spatial resolution on the order of 20 μm, for the velocity components in the axial and transverse directions, both at the junction and at different axial displacements on either side of the junction. The data have been compared with solutions of the Navier-Stokes equations obtained by finite difference numerical methods using a Macintosh personal computer. Excellent agreement is apparent without the need for any adjustable parameters, the numerical solutions depending only on the Reynolds number determined from inlet flow conditions. This study demonstrates the usefulness of dynamic NMR microscopy for the study of the flow of Newtonian fluids in complex geometries. The method can also be applied to the flow of non-Newtonian fluids.

Introduction

The ability to measure velocity profiles experimentally is important in both engineering fluid dynamics and rheology. In the study of Newtonian fluids, where the Navier-Stokes equations are believed to contain all of the basic physics, experimental determinations of the velocity profile allow engineers and applied mathematicians to check numerical methods of solutions of these equations for complex geometries. In rheological studies of non-Newtonian fluids, the constitutive equations describing the relationship between stress and strain must be validated by comparing theory with experiment. Measurements of the components of the velocity for relatively simple geometries provide excellent tests of any proposed constitutive equation. Several techniques (Emrich, 1981) such as chronophotography, laser Doppler velocimetry and hot-wire anemometry are available to visualize the flow but few are able to provide precise and accurate measurement over a wide field in a noninvasive way. For example, flow visualization can be achieved using a high-speed camera to photograph fluid doped with foreign tracer dopants, such as dye or fine aluminium dust. While chronophotography allows the simultaneous visualization of a wide velocity field, the dye-doping method suffers from diffusive spreading after injection and therefore can only provide a qualitative picture of the flow. The aluminium dust method could provide a quantitative measurement, but it is based on the assumption that the tracer particles follow the local fluid flow exactly. This key assumption is questionable when the density of these particles is different from that of the surrounding fluid. The situation is even more complicated when one considers the response of tracer particles to sudden velocity variations such as local secondary flows. Such effects are likely to be worse for low viscosity fluids such as water. The velocity profile can also be measured using high-resolution laser Doppler velocimetry but this method still requires uniformly-sized fine particles to serve as scattering centers in the fluid and can fail near the wall of the tube due to the anomalous scattering of the laser beam. Furthermore, laser Doppler velocimetry measures the velocity one point at a time and to map an entire velocity field for a complex geometry means altering the experimental set up for each measurement. Hot-wire anemometers suffer in comparison to other techniques because a probe must be inserted into the fluid and

Correspondence concerning this article should be addressed to P. T. Callaghan.

there is a nonlinear relation between the input and output of the detector.

A newly-developed imaging technique, which has been called Dynamic NMR Microscopy (Callaghan et al., 1988, Callaghan, 1991), offers a number of advantages over all the conventional methods. This technique is capable of simultaneously constructing both velocity and self-diffusion images of the sample. It is able to provide a velocity resolution of a few tens of microns per second and a spatial resolution of a few tens of microns. Furthermore, it is a totally noninvasive technique and requires no particulate dopant in the fluid. Recent applications using this technique include studies of laminar water flow through capillary tubes (Callaghan and Xia, 1991), non-Newtonian fluid flow in polymer solutions (Xia and Callaghan, 1991), flow in a hollow-fiber bioreactor (Heath et al., 1990), vascular water flow imaging in plants in vivo (Köckenberger et al., 1992), and bulk water flow in wheat grain in vivo (Jenner et al., 1988).

This article deals with the problem of laminar flow through an axisymmetric sudden expansion or contraction. This problem has long been of both theoretical and experimental interest. There have been a number of studies designed to investigate the growth of the shear layer between the central set and the reverse flow along the wall in the region of the separated flow. The axial extent of the flow separation region and the location of the flow reattachment is determined by the lateral growth or spreading of the shear layer. An excellent summary of this work appears in the introduction to the article by Latornell and Pollard (1986). For example in the work of Macogno and Hung (1967) the flow at the expansion was observed by dispersing fine tracer particles (aluminium powder) in oil and photographing the streamlines. The photographic information was supplemented with direct visual observations of dyed oil injected into the flow through a series of small holes bored in the walls of the pipe. While some velocity profiles across the pipes were calculated, comparisons with experiment could not be carried out. Instead several visual flow characteristics were determined, such as the flow reattachment length, the location of the eddy center, the relative eddy intensity and the relative maximum vorticity in the backflow region. Comparisons of the theoretical and experimental values of these characteristics showed excellent agreement.

It should be noted that the studies referred to have compared theoretical predictions with the results of flow visualization. The current work was undertaken in order to demonstrate that Dynamic NMR Microscopy can obtain accurate numerical measurements of the velocity field in complex geometries. Measurements of the velocity in water flowing at low Reynolds number through tubes exhibiting an abrupt contraction and an abrupt expansion were carried out. Simulations based on numerical solutions of Navier-Stokes equations using finite difference methods were made to compare the measurements with the theoretical velocity distributions. These simulations were carried out on a personal computer. This article demonstrates that it is possible to obtain entire velocity profiles for complex geometries to test numerical solutions of the Navier-Stokes equations for engineering applications and to test constitutive equations for non-Newtonian fluids.

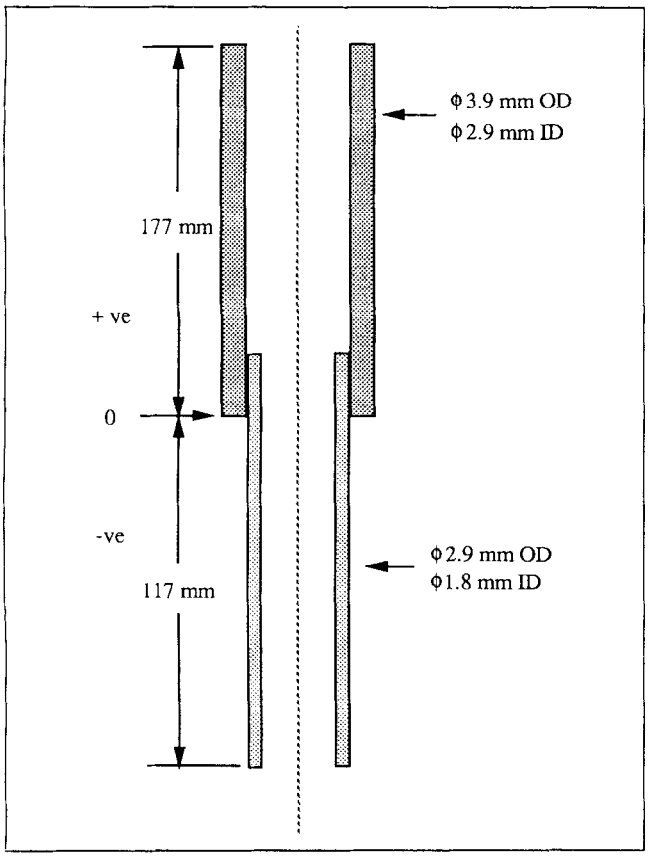

Figure 1. Stepped tube used to provide both the abrupt contraction and expansion in the water flow.

Theory

The flow configurations in which we are interested are the 'abrupt contraction' and the 'abrupt expansion' geometries. The physical arrangement of the two tubes forming the contraction and expansion are shown in Figure 1. The two arrangements were obtained by reversing the direction of flow. While the experiments described here are performed with low Reynolds numbers where the flow is expected to be highly laminar, some secondary flow is expected in the vicinity of the shape corners. Of particular interest in this work is the velocity field in the vicinity of the junction of the two tubes.

In describing fluid flow in circular cross-sectional tubes it is convenient to use cylindrical coordinates. The analysis can be further simplified by noting the azimuthal symmetry inherent in the geometry at low Reynolds number. By setting all azimuthal variations to zero, the problem reduces to two dimensions. For an incompressible fluid with constant viscosity, the continuity equation and the Navier-Stokes equations expressed in cylindrical coordinates are:

$$\frac{\partial v_r}{\partial r}+\frac{v_r}{r}+\frac{\partial v_z}{\partial z}=0 \tag{1}$$

$$\frac{\partial v_r}{\partial t}+v_r\frac{\partial v_r}{\partial r}+v_z\frac{\partial v_r}{\partial z}=-\frac{1}{\rho}\frac{\partial P}{\partial r}+\nu\left\{\frac{\partial}{\partial r}\left[\frac{1}{r}\frac{\partial}{\partial r}(rv_r)\right]+\frac{\partial^2 v_r}{\partial z^2}\right\} \tag{2}$$

$$\frac{\partial v_z}{\partial t}+v_r\frac{\partial v_z}{\partial r}+v_z\frac{\partial v_z}{\partial z}=-\frac{1}{\rho}\frac{\partial P}{\partial z}+\nu\left[\frac{1}{r}\frac{\partial}{\partial r}\left(r\frac{\partial v_z}{\partial r}\right)+\frac{\partial^2 v_z}{\partial z^2}\right] \tag{3}$$

where ν and ρ are the kinetic viscosity and the density of the

fluid, respectively, their product, $\nu\rho$, is equal to the dynamic viscosity of the fluid, μ. The radial and axial components of the velocity are v_r and v_z while P is the pressure.

For steady-state flow far from the junction region, the radial velocity and the rate of the change of the axial velocity are zero. In this limit, the above equations reduce to:

$$\frac{\mu}{r}\frac{d}{dr}\left(r\frac{dv_z}{dr}\right)=\frac{dP}{dz} \tag{4}$$

where dP/dz is the axial pressure gradient. Given the usual boundary conditions of no-slip at the wall ($v_z|_{r=r_0} = 0$) and radial symmetry on the center line,

$$\frac{\partial v_z}{\partial r}|_{r=0}=0,$$

the solution for the above equation yields the classical Poiseuille velocity profile:

$$v_z(r)=v_{\max}\left(1-\frac{r^2}{r_0^2}\right) \tag{5}$$

where r_0 is the radius of the tube and $v_{\max}$ is the maximum velocity found on the center line of the tube.

Numerical Solution to Navier-Stokes Equations

In order to describe the flow in the junction region it is necessary to solve Eq. 1 to 3. Because of the complex geometry in the junction region, analytical solutions are not possible and numerical methods must be used. There are several well established procedures for the numerical solution of the Navier-Stokes equations (Roache, 1972; Peyret and Taylor, 1983; Fletcher, 1988). One method which is relatively easy to develop and program uses the stream function-vorticity formulation of Eqs. 1 to 3 instead of the primitive variables; v_r, v_z and P. The equation of continuity Eq. 1 is exactly satisfied by introducing the stream function and the convergence of finite difference methods is usually rapid. The stream function, Ψ, and the vorticity function, Ω, are defined by:

$$v_z=-\frac{1}{r}\frac{\partial\Psi}{\partial r} \tag{6a}$$

$$v_r=\frac{1}{r}\frac{\partial\Psi}{\partial z} \tag{6b}$$

and

$$\Omega=\frac{\partial v_r}{\partial z}-\frac{\partial v_z}{\partial r}. \tag{7}$$

It is useful to express the equations in nondimensional form by introducing an appropriate length and velocity scale. Lengths are expressed in terms of the radius of the inlet tube, R_{in}, and velocities in terms of the maximum axial velocity at the inlet, V_{in}. The dimensionless forms of the stream function, vorticity and time are:

$$\Phi=\frac{\Psi}{R_{\text{in}}^2V_{\text{in}}} \tag{8}$$

$$\omega=\frac{\Omega R_{\text{in}}}{V_{\text{in}}} \tag{9}$$

$$t=\frac{TV_{\text{in}}}{R_{\text{in}}}. \tag{10}$$

The resulting dimensionless Navier-Stokes equations for the stream function and vorticity are:

$$\left[\frac{\partial^2}{\partial r^2}-\frac{1}{r}\frac{\partial}{\partial r}+\frac{\partial^2}{\partial z^2}\right]\Phi=\omega r \tag{11}$$

and

$$\frac{\partial\omega}{\partial t}+\frac{\partial(v_z\omega)}{\partial z}+\frac{\partial(v_r\omega)}{\partial r}=\frac{1}{Re}\left[\frac{\partial^2}{\partial r^2}+\frac{1}{r}\frac{\partial}{\partial r}-\frac{1}{r^2}+\frac{\partial^2}{\partial z^2}\right]\omega \tag{12}$$

where Re is the Reynolds number, given by:

$$Re=\frac{V_{\text{in}}R_{\text{in}}}{\nu}. \tag{13}$$

Equations 11 and 12 along with the nondimensional forms of Eq. 6 can be used to calculate the velocity distributions for the chosen geometries by applying appropriate boundary conditions and the conservation of the volume flow:

$$V_{\text{in}}R_{\text{in}}^2=V_{\text{out}}R_{\text{out}}^2 \tag{14}$$

where R_{out} and V_{out} are the radius and maximum velocity for the outlet tube in the region far from the junction. Fully developed Poiseuille flow is assumed far away from the junction region so that v_r, v_z, Φ, and ω are all defined at the inlet and outlet. As pointed out by Tanner (1985) for axially symmetric creeping flows the flow field along the axis must be investigated over lengths greater than twice the radius. At larger Reynolds numbers the region investigated either side of the junction, especially down stream, must be larger. On the center line v_r and ω are zero while Φ is a constant. The axial velocity v_z must be determined on the center line where $r \to 0$ but the use of L'Hopital's rule shows that:

$$v_z=-\frac{\partial^2\Phi}{\partial r^2} \tag{15}$$

On the walls of the tubes, v_r and v_z (no slip condition) are equal to zero and Φ is a constant which is set equal to zero. The vorticity must be calculated at each point along the wall and often it is the manner in which this problem is handled that determines the success of any numerical evaluation of the Navier-Stokes equations. On the walls Φ and $d\Phi/dr$ both equal zero and from these relationships first-order or second-order formulae (Peyret and Taylor, 1983) relating the vorticity on the boundary to the stream function in the near vicinity can be derived from Eq. 11. At the junction of the two tubes, there are special problems at the corners. Moffatt (1964) has shown

that ω is singular at a sharp corner and there is a thorough discussion of this point in the book by Crochet et al. (1984); but again it is possible to express ω in terms of Φ.

Because v_r and v_z are expressed in terms of Φ in Eq. 6, only Eqs. 11 and 12 for Φ and ω need be solved, but because ultimately v_r and v_z are to be determined it is convenient to include these at each cycle of the iterative process. An iterative procedure must be used to solve the coupled set of Eqs. 11 and 12 for Φ and ω. The stream function is updated from the previous values of the vorticity using Eq. 11 and then the vorticity is updated using Eq. 12 and the velocities calculated from the previous values of the stream function. The question arises as to how the individual Eqs. 11 and 12 should be solved. There are explicit methods and relaxation techniques (Press et al. 1989). The relaxation methods are convenient in this case because they are relatively simple to program and what is more important, because the overall solution is iterative, it is not necessary to carry the relaxation solutions of the individual equations to completion within each cycle.

To cast the fluid mechanical equations into a set of finite difference equations a grid of points in the r, z plane is defined and the derivatives replaced by second-order central differences. The velocities v_r and v_z can be determined from the stream function using the relations:

$$v_{r\ n,m} = (1/2hr)(\Phi_{n,m+1} - \Phi_{n,m-1}) \tag{16}$$

$$v_{z\ n,m} = -(1/2hr)(\Phi_{n+1,m} - \Phi_{n-1,m}) \tag{17}$$

where h is the separation between grid points. On the center line ($n = 0$), the second-order equation derived from Eq. 15:

$$v_{z\ 0,m} = -(1/2h^2)(7\Phi_{0,m} + \Phi_{2,m} - 8\Phi_{1,m}) \tag{18}$$

was used. Equation 11 for the stream function can be written:

$$\Phi^*_{n,m} = (1/4)\{\Phi_{n,m+1} + \Phi_{n,m-1} + (1\text{-}h/2r)\Phi_{n+1,m} + (1 + h/2r)\Phi_{n-1,m} - h^2 r\omega_{n,m}\} \tag{19}$$

where n and m label the grid points in the radial and axial directions respectively. Provided $\omega_{n,m}$ is known at each grid point Eq. 19 can be solved using relaxation techniques (Press et al., 1989) where each iteration is stepped forward using the equation:

$$\Phi^{k+1}_{n,m} = \Phi^k_{n,m} + RF_\Phi(\Phi^*_{n,m} - \Phi^k_{n,m}) \tag{20}$$

and RF_Φ is a relaxation factor. This method of solution is stable provided $0 < RF_\Phi < 2$. Because a steady state solution for the Navier-Stokes equations is desired, Eq. 12 for the vorticity can be solved as a parabolic system with a time dependent method in which the number of time steps is large enough to allow the system to come to the steady state or as an elliptic system using iterative techniques (Peyret and Taylor, 1983). The two methods are very similar. For the steady state solution, the vorticity at one step is related to the vorticity at the previous one by the relation:

$$\omega^{k+1}_{n,m} = \omega^k_{n,m} + RF_\omega(\omega^*_{n,m} - \omega^k_{n,m}) \tag{21}$$

where

$$\omega^*_{n,m} = (1/k_0)\{k_1\omega_{n+1,m} + k_2\omega_{n-1,m} + k_3\omega_{n,m+1} + k_4\omega_{n,m-1}\} \tag{22a}$$

and

$$k_0 = 4 + (h/r)^2 \tag{22b}$$

$$k_1 = (1 + h/2r) - (hRe/2)v_{r\ n+1,m} \tag{22c}$$

$$k_2 = (1 - h/2r) + (hRe/2)v_{r\ n-1,m} \tag{22d}$$

$$k_3 = 1 - (hRe/2)v_{z\ n,m+1} \tag{22e}$$

$$k_4 = 1 - (hRe/2)v_{z\ n,m-1} \tag{22f}$$

This relaxation method converges provided that the factor $hRe/2 < 1$ and the relaxation factor RF_ω is such that $0 < RF_\omega < 2$. For $Re < 100$ the grid can be made fine enough (that is, h small enough) that stability is ensured. One approach to reducing the difficulty arising at large Re is to use an upwind noncentered approximation (Torrance, 1968) for the convective term:

$$\frac{\partial(v_z\omega)}{\partial z} + \frac{\partial(v_r\omega)}{\partial r}$$

in Eq. 12.

On the boundaries the vorticity was updated using:

$$\omega^{k+1}_{n,m} = \omega^k_{n,m} + RFB_\omega(\omega^*_{n,m} - \omega^k_{n,m}) \tag{23}$$

where RFB_ω is a relaxation factor satisfying the condition $0 < RFB_\omega < 2$. On the portion of the walls of the tubes parallel to the flow, the second-order equation (Jensen, 1959):

$$\omega^*_{n,m} = -(1/2h^2r)(8\Phi_{n-1,m} - \Phi_{n-2,m}) \tag{24}$$

was used. At the step where the tube wall is perpendicular to the flow:

$$\omega^*_{n,m} = -(1/2h^2r)(8\Phi_{n,m+1} - \Phi_{n,m+2}) \tag{25}$$

At the re-entrant corner the method of Kawaguti (1969) was used and:

$$\omega^*_{n,m} = -(2/h^2r)(\Phi_{n,m+1} + \Phi_{n-1,m}) \tag{26}$$

At the internal corner the vorticity was set equal to zero.

A flow chart for the numerical simulation is as follows:

Step 1. Determine the grid size to be used for the computations of the Reynolds number, the relaxation factors, RF_Φ, RF_ω and RFB_ω, and the residual limits ϵ_Φ and ϵ_ω.

Step 2. Set the fixed boundary conditions for v_r on all boundaries, v_z at inlet, outlet and walls, Φ on all boundaries, and ω at inlet, outlet and center line.

Step 3. Set the initial values for Φ and ω at all other points.

Step 4. Use Eqs. 19 and 20 to calculate new values for $\Phi_{n,m}$. Repeat this step until the sum of the absolute value of the changes in Φ is less than ϵ_Φ but limit the number of relaxation steps to 10.

Step 5. Calculate v_r and v_z using Eqs. 16, 17 and 18.

Step 6. Update ω using Eq. 21 in conjunction with Eq. 22. On the boundary use Eq. 23 and the appropriate one of Eqs. 24, 25 and 26. Repeat this step but traverse the grid of points in the opposite direction.

Step 7. Check for convergence. Stop if the sum of the changes in ω is less than ϵ_ω otherwise return to step 4.

Figure 1 shows the physical layout of the junction region used in the flow measurements. In the simulations it was found convenient to use a square grid 0.05 mm on a side and the grid extended from 3 mm upstream to 7 mm downstream. Programs were written in Pascal for a Macintosh SE/30 Apple Computer (Cupertino CA USA) using the Think Pascal compiler (Symantic Corp. Cupertino CA USA). It was found by experience that convergence with ϵ_Φ and ϵ_ω set equal to 0.0001 could be achieved for values of *Re* between 1-50 in 50-200 iterations through steps 4-7. With these values of ϵ_Φ and ϵ_ω the calculated values of the velocities stabilized to with 1% and reducing ϵ_Φ and ϵ_ω further greatly increased the number of iterations. The value of RF_Φ was set to 1.0 and it was found that step 4 was repeated only once or twice per iteration after the first few had been carried out. A considerable reduction (50%) in the number of cycles through steps 4-7 could be achieved by using over relaxation in the calculation of the vorticity. By trial and error, RF_ω and RFB_ω were increased from 1 and it was found that the number of iterations necessary for a fixed reduction in the residuals went through a minimum. Generally a calculation of the velocities for a particular *Re* took about 10 minutes on the Macintosh SE/30.

The initial values of Φ and ω were normally set to values calculated for Poiseuille flow appropriate far from the junction region. Other calculations were carried out setting Φ and ω equal to zero away from the boundary to check that the same final velocities were reached regardless of the initial conditions. As a further verification of the simulation results, the program was modified to evaluate the vorticity at each iteration using the time dependent equation and following the time course to equilibrium. Another modification involved treating each square of the grid as a cell (Takemitsu, 1985) where the stream function and vorticity are defined on the corners and the velocities midway along the sides. These variations in the basic program all lead to the same final results.

Dynamic NMR Microscopy

Following the initial suggestion of imaging nuclear spin density using magnetic field gradients (Lauterbur, 1973; Mansfield and Grannell, 1973), Nuclear Magnetic Resonance imaging (NMR imaging or MRI) has been widely used in scientific research and medical tomography (Morris, 1986). Where the resolution of the image voxel is smaller than $(0.1\ \text{mm})^3$, such tomography may be termed 'NMR microscopy' (Callaghan, 1991) simply because this volume is the smallest which can be resolved using the human eye. At the present, the best resolution in NMR imaging is about 10 μm^3. However, the value of NMR imaging is less in its microscopic resolution than in the noninvasive nature of the measurement and the fact that the images can be made sensitive to factors other than the density of resonant spins such as the spin-spin or spin-lattice relaxation times, chemical-shift, or molecular motion.

The fundamental principles of NMR imaging are well known and based on the simple fact that the nuclear precession frequency, known as Larmor frequency, is proportional to the magnitude of the external polarizing magnetic field at the nuclear site. When the external magnetic field varies spatially, the Larmor frequency of the nuclear spins will differ from one location to another across the sample so that spatial position is encoded by a frequency given by:

$$\omega(\mathbf{r}) = \gamma B_0 + \gamma \mathbf{G} \cdot \mathbf{r} \tag{27}$$

where B_0 is the polarizing magnetic field, γ is the gyromagnetic ratio of the nucleus and G is the spatial mapping gradient vector. Three orthogonal gradients are sufficient to locate the spins anywhere in real space. In practice, it is convenient to select a 'thin' slice of spins by selective excitation of only those spins in a particular plane and spatial encoding of the spins in this plane is then performed with two mutually perpendicular gradients. This technique reduces the data array to two dimensions which is consistent with the final 2-D presentation of an image. One possible sequence of radio frequency and magnetic field gradient pulses that can be used for NMR imaging in a selected plane is shown in Figure 2a.

In NMR imaging experiments, it is convenient to define a reciprocal space vector:

$$\mathbf{k} = (2\pi)^{-1} \gamma \mathbf{G} t. \tag{28}$$

It can be shown (Callaghan, 1991) that the nuclear signal determined in an NMR imaging experiment is given by:

$$S(\mathbf{k}) = \int \rho(\mathbf{r}) \exp(i 2\pi \mathbf{k} \cdot \mathbf{r}) d\mathbf{r} \tag{29}$$

where $\rho(r)$ is the local nuclear spin density. Therefore the spin density, $\rho(r)$, is simply related to the time domain signal, $S(k)$ via a Fourier transformation. The image reconstructed using Eq. 29 is sometimes termed the (static) k-space image, because it represents a time-independent function, $\rho(r)$.

In order to probe the translational motion of the nuclear spins a narrow Pulsed-Gradient Spin-Echo (PGSE) sequence shown in Figure 2b is inserted into the usual imaging sequence. The combination of the PGSE contrast scheme and the static NMR imaging is termed Dynamic NMR Microscopy. Figure 2c shows a typical pulse sequence for a dynamic NMR imaging experiment. In the PGSE sequence shown in Figure 2b, a dephasing of the spins arises because of the imposition of a magnetic field gradient. The subsequent rephasing of the dephased spins requires an identical gradient pulse following the phase inverting 180° pulse. The signal from any stationary spins will be refocused perfectly but any motion during the time Δ will shift a spin to a new location and will result in a different Larmor frequency. Following a similar approach used before in the static NMR imaging, a dynamic reciprocal space vector, q, is defined by:

$$\mathbf{q} = (2\pi)^{-1} \gamma \mathbf{g} \delta. \tag{30}$$

Even at microscopic resolution, NMR microscopy still probes a molecular ensemble because each voxel element contains a large number of molecules. The function governing the motion of these molecular ensembles is an averaged propagator,

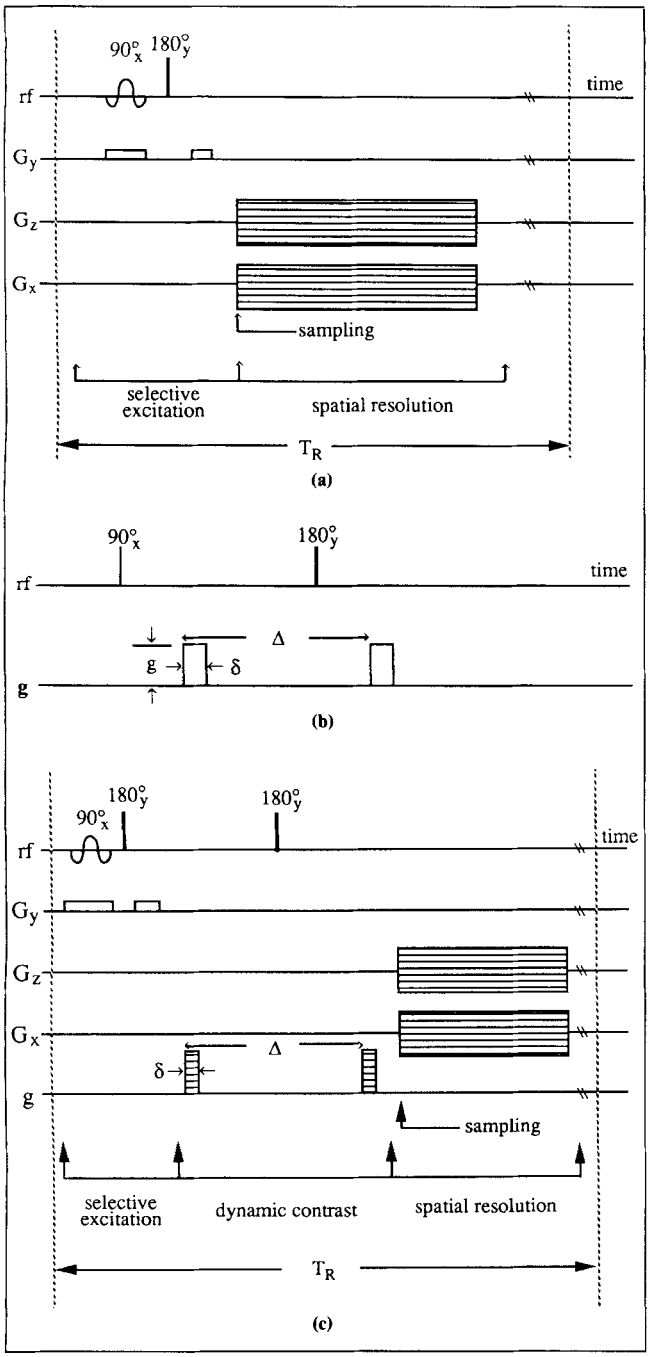

Figure 2. Nuclear magnetic resonance imaging pulse sequences.

(a) the pulse sequence used to obtain static two-dimensional images of the proton spin density distribution within a selected slice perpendicular to the flow; (b) the standard pulsed gradient spin echo, PGSE, sequence used to measure bulk velocity and diffusion; (c) a dynamic NMR imaging pulse sequence used to obtain two-dimensional maps of both velocity and diffusion.

$\overline{P_s}(\boldsymbol{R},\Delta)$, giving the probability that a spin, anywhere in the sample, has moved by $\boldsymbol{R}$ in a time Δ. Thus the normalized echo signal resulting from a PGSE pulse sequence can be shown to be:

$$E_\Delta(\mathbf{q}) = \int \overline{P_s}(\mathbf{R},\Delta)\exp(i2\pi\mathbf{q}\cdot\mathbf{R})d\mathbf{R} \tag{31}$$

where $E_\Delta(q)$ is the echo signal amplitude normalized to the amplitude when $q=0$.

The propagator, $\overline{P_s}(\boldsymbol{R},\Delta)$, is related to the normalized echo signal via a Fourier transformation. When the gradient pulse width is narrow, and both translational flow and random Brownian motion occur, an analysis of Eq. 31 leads to a simple result: the normalized echo signal is a product of a phase shift term and an amplitude attenuation term.

$$E_\Delta(\mathbf{q}) = \exp(i2\pi q v\Delta)\exp(-4\pi^2 q^2 D\Delta) \tag{32}$$

where v is the velocity in the direction of q and D is the self-diffusion coefficient.

By combining the PGSE sequence with the normal imaging pulse as shown in Figure 2c, the PGSE sequence serves as a precursor to imaging and imposes a spatially-varied dynamic contrast to the static image density so that the 'dynamic time-domain' signal is given by:

$$S(\mathbf{k},\mathbf{q}) = \int E_\Delta(\mathbf{q})\rho(\mathbf{r})\exp(i2\pi\mathbf{k}\cdot\mathbf{r})d\mathbf{r} \tag{33}$$

The direction of q determines the component of the velocity which is to be measured. Although in general the q gradient can be applied in any direction, for practical reasons a single dimension in q space is probed at any one time. Since slice selection is used the over-all imaging process is three dimensional within the plane being examined. By varying the k gradient a complex pair of planar images weighted by $E_\Delta(q)$ is reconstructed by filtered back projection for each value of q. Figure 3a shows a sequence of images for a set of q values for Poiseuille flow in a cylindrical tube, the direction of q being along the direction of flow. Subsequent Fourier transformation in q space using the multiple q-contrasted slices produces $\overline{P_s}(\boldsymbol{R},\Delta)$ at each pixel of the image. As shown in Figure 4, $\overline{P_s}$ is a Gaussian curve centered at $v\Delta$ and the width of the curve is proportional to the square root of the self-diffusion coefficient of the molecules. It can be shown (Callaghan and Xia, 1991) that the velocity and self-diffusion values in SI units are given by:

$$v = \frac{2\pi n_D k_v}{N\gamma g_m \delta\Delta} \tag{34}$$

and

$$D = \frac{3.56(n_D k_{FWHM})^2}{\gamma^2 N^2 g_m^2 \delta^2 \Delta} \tag{35}$$

where N is the digital array size in transformation, g_m is the maximum PGSE gradient applied, n_D+1 is the total number of q slices in the experiment, k_v is the position of the peak and k_{FWHM} is the peak width. In practice, the number of q slices, n_D, is small (12 to 18 in our experiments) while the digital array size, N is a large number, for example 256. This arrangement is used to avoid excessive long times collecting data but still keep the necessary digital precision in the data analysis. Our analysis shows that the precision in determining k_v is of order ± 2 in the velocity digital range from -128 to 127.

Experimental Apparatus and Method

Dynamic NMR imaging experiments were carried out using

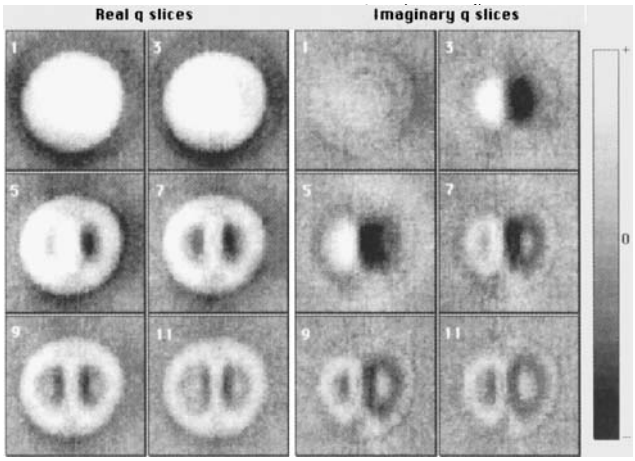

(a)

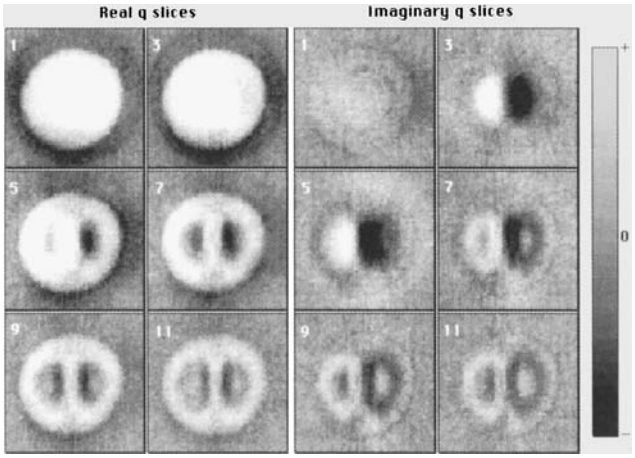

(b)

Figure 3. Selection of both the real and imaginary images for a set of q values.

In general 18 pairs were collected but only the odd numbered pairs 1 through 11 are shown. (a) The images are for flow far from the junction region where Poiseuille conditions prevail and q is directed axially; (b) the vector q is directed transverse to the flow and the slice center is located at the abrupt junction.

a micro-imaging system based on a modified JEOL FX-60 spectrometer and a 6-in. (152-mm) electromagnet with a 1.25-in. (32-mm) gap. The static magnetic field from the electromagnet defines the z direction in the laboratory frame of reference. The imaging probe hosts a set of gradient coils with G_x, G_y and G_z gradients and these three gradient coils were driven separately by three KEPCO programmable power supplies. The vertically directed G_y gradient was in the direction of net flow while the G_x and G_z gradients were in the plane perpendicular to the direction of flow. The digital array size for these imaging experiments was 64 × 64.

The stepped tube was made using two pieces of glass capillary with the internal diameters of 2.9 mm and 1.8 mm, respectively, as shown in Figure 1. The end of the small-diameter tube was hand-polished to be smooth and flat, and then fitted tightly into the large-diameter tube to form an abrupt junction. This junction was then sealed using glue and teflon tape. Both ends of the stepped tube were connected to glass beakers (5 l in volume and 21 cm in diameter) using plastic tubes. A 3.25-m-long small diameter plastic tube (0.9-mm ID) was also connected in series with the sample tube to deliberately increase the 'resistance' to the water flow. Constant water flow was established by maintaining the height difference of two glass beakers to a constant value. The stepped tube was placed vertically through the imaging probe and the contraction and expansion flow conditions were achieved by changing the direction of flow. Flow reversal was achieved by changing the relative heights of the inlet and outlet water tanks leaving the stepped tube untouched. The water sample was doped with 0.1% $CuSO_4$ to decrease the spin-lattice relaxation time so that the data could be collected more rapidly.

The integrated volume flow during one imaging experiment was less than 250 mL and caused a maximum change of 4% in the level of the water in the reservoirs. It should be noted that the impact of any level change during the experiment is reduced because the q slices are acquired with increasing PGSE gradient. This increases the effect of diffusive motion so that the image intensities of the q slices become progressively weaker. Therefore, any error occuring during the latter part of the imaging experiment has much less influence on the subsequent Fourier analysis.

The NMR signal was acquired on resonance so that the slice selected through the stepped tube was always at the center of the probe. However, the vertical position of the junction inside the imaging probe could be located by rotating a screw adjustment. The junction was labelled as the zero position and the direction of flow defines the positive direction. At each position, a sequence of images were obtained for a set of q values. Filtered back projection was performed using 60 values of the mapping gradient in the x-z plane. The magnitude of the maximum mapping gradient applied in the x-z plane remained unaltered during all the imaging experiments in order to simplify data analysis. To measure the axial component of the fluid velocity the PGSE gradient was applied along the y direction, the direction of flow, and the thickness of the plane perpendicular to the flow investigated was 0.33 mm. The PGSE pulse separation, Δ, was 5 ms and the maximum q gradient was 0.936 T m^{-1}. A PGSE pulse duration time of 2.5 ms was used when flow in the large diameter tube was being examined while 1.0 ms was used for the faster flow prevailing in the small diameter tube. To measure the transverse component of the fluid velocity the PGSE gradient was applied along the x direction. For these measurements the slice thickness was set to 0.66 mm in order to enhance the signal to noise ratio. The PGSE pulse separation was 13 ms, PGSE pulse duration 9 ms and maximum q gradient 0.13 T m^{-1}.

A selection from a typical set of q space images used to determine the transverse component of the velocity are shown in Figure 3b. Based on the azimuthal symmetry assumption, the radial velocity component is taken to be the transverse component in the diametrical slice parallel to the gradient. For both the transverse and axial measurements 18 successive real and imaginary images were obtained as q was increased by stepping the PGSE gradient in 18 intervals from zero to the maximum gradient. The individual pixels within the q space images exhibit the modulation described by Eq. 32. The velocities at each point within the selected plane were then obtained by Fourier transforming the signal from each pixel to obtain the Gaussian curve such as shown in Figure 4. The data set of 18 points for each pixel (one for each q value) were zero filled to 256 before the Fourier transformation. From the po-

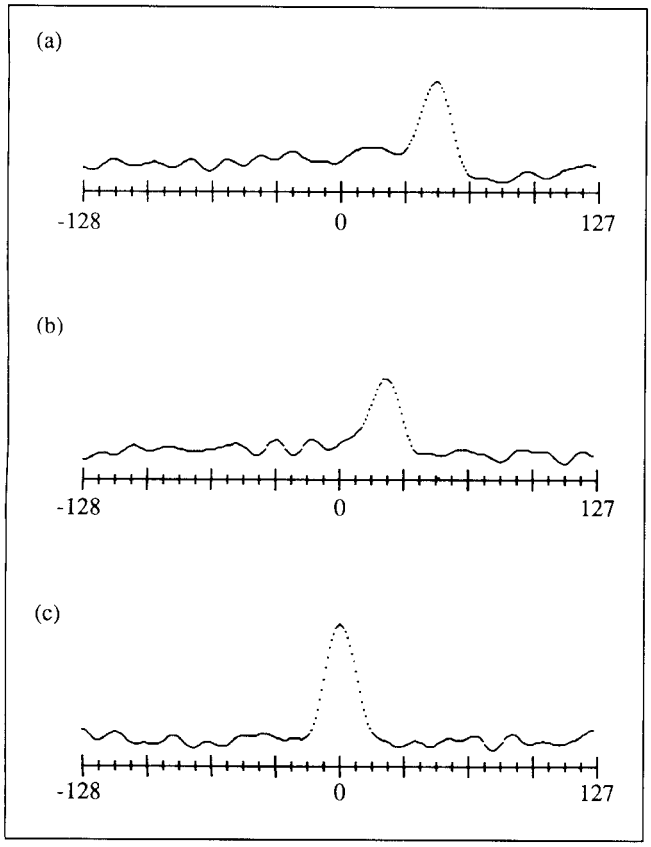

Figure 4. Using the images for a set of q values such as those in Figure 3, the dynamic displacement profiles can be obtained for each pixel by a Fourier transformation.

The displacement of the center of the Gaussian peak from the origin gives the velocity for that particular pixel. The width of the peak is proportional to the molecular self diffusion coefficient. The three dynamic displacement profiles correspond to different pixels in which the k_v and k_{FWHM} values are respectively: (a) 48 and 14 digits, (b) 24 and 15 digits, and (c) 0 and 14 digits. The corresponding velocities and self-diffusion coefficients can be calculated using Eqs. 34 and 35.

sition of the peak and the width of the Gaussian curve the velocity and the diffusion coefficient were determined for each pixel using Eqs. 34 and 35. The resulting data could be displayed as a velocity or diffusion map for a particular plane perpendicular to the axis of the tube such as those shown in Figure 5.

A series of imaging experiments were performed for different positions of the stepped tube to map the axial and radial velocities in the junction region at the ambient temperature of the probe which was around 30°C. The data collection for a complete mapping of the velocity in one plane at a particular position along a tube took about 3 hours to complete. Because the flow patterns explored in these experiments are essentially two-dimensional (axial and radial), it was not necessary to collect data for the entire plane. It would have been sufficient to obtain data along a single direction perpendicular to the flow to obtain the axial and radial velocity profiles at a single position along the tube and such an experiment could in principle be carried out in less than 10 minutes.

Results

q space images

The real and imaginary images obtained for a succession of increasing PGSE gradients along the axial direction are shown in Figure 3a for the case of flow far from the junction. The "phase rings" seen in the images are a result of the Poiseuille flow conditions and the circular symmetry of the images indicates that there is no azimuthal dependence of the flow. As the PGSE gradient, q, is made larger the phase shift factor $\exp(i2\pi qv\Delta)$ from Eq. 32 increases and as a consequence the number of rings observed within the image increases. There is a gradual decay of the image amplitude with increasing q as well, due to the diffusive factor $\exp(-4\pi^2q^2D\Delta)$. Far from the junction region where Poiseuille conditions prevail there is no radial component to the velocity and application of the PGSE gradient along the x direction produces a null result. Figure 3b shows the q space images for a determination of the radial velocity in the junction region. In this case the flow is being forced from a larger to a smaller tube and the radial velocity is inward toward the center of the tube. The double lobe structure that appears in the images is a consequence of the fact that the PGSE gradient is along a single direction transverse to the tube axis.

Velocity profiles

After Fourier transforming the data for each pixel in the q space images, a set of velocity maps such as those shown in Figure 5 were obtained. The flow of water through both the tube contraction and expansion are essentially two-dimensional problems in fluid dynamics and therefore the data from the experimental measurements can be displayed as plots of radial and axial velocity as functions of position measured from the center line of the tubes. The experimental results in this format are shown in Figures 6 and 7. The curves for the radial velocity are antisymmetric because the velocity is measured along a single coordinate axis rather than radially. For contraction, radial velocities are directed inward and are outward for expansion.

From repeated measurements it is estimated that the values for the axial velocities displayed in Figures 6 and 7 are known with an associated error of about 2% of the maximum, that is, 0.4 mm/s. As a check of precision, the maximum values of the velocity at the center of the tubes far from the junction region should be in the ratio of the square of the tube diameters. The tube diameters were measured to be 1.80 ± 0.01 and 2.90 ± 0.01 mm and the ratio of the diameters squared is therefore 0.385 ± 0.008. For the contraction configuration the inlet and outlet velocities on the center line were 6.7 and 18.7 mm/s with the resulting ratio of 0.360 ± 0.014. For expansion the velocities were measured to be 18.0 and 6.7 mm/s resulting in the ratio 0.372 ± 0.014. The radial velocities are more difficult to measure because they are a factor of 10 smaller than the axial velocities. It is estimated that the error associated with the radial velocities is 5%.

Discussion

In the regions far from the junction the characteristic features of Poiseuille flow are observed. The axial velocity profiles

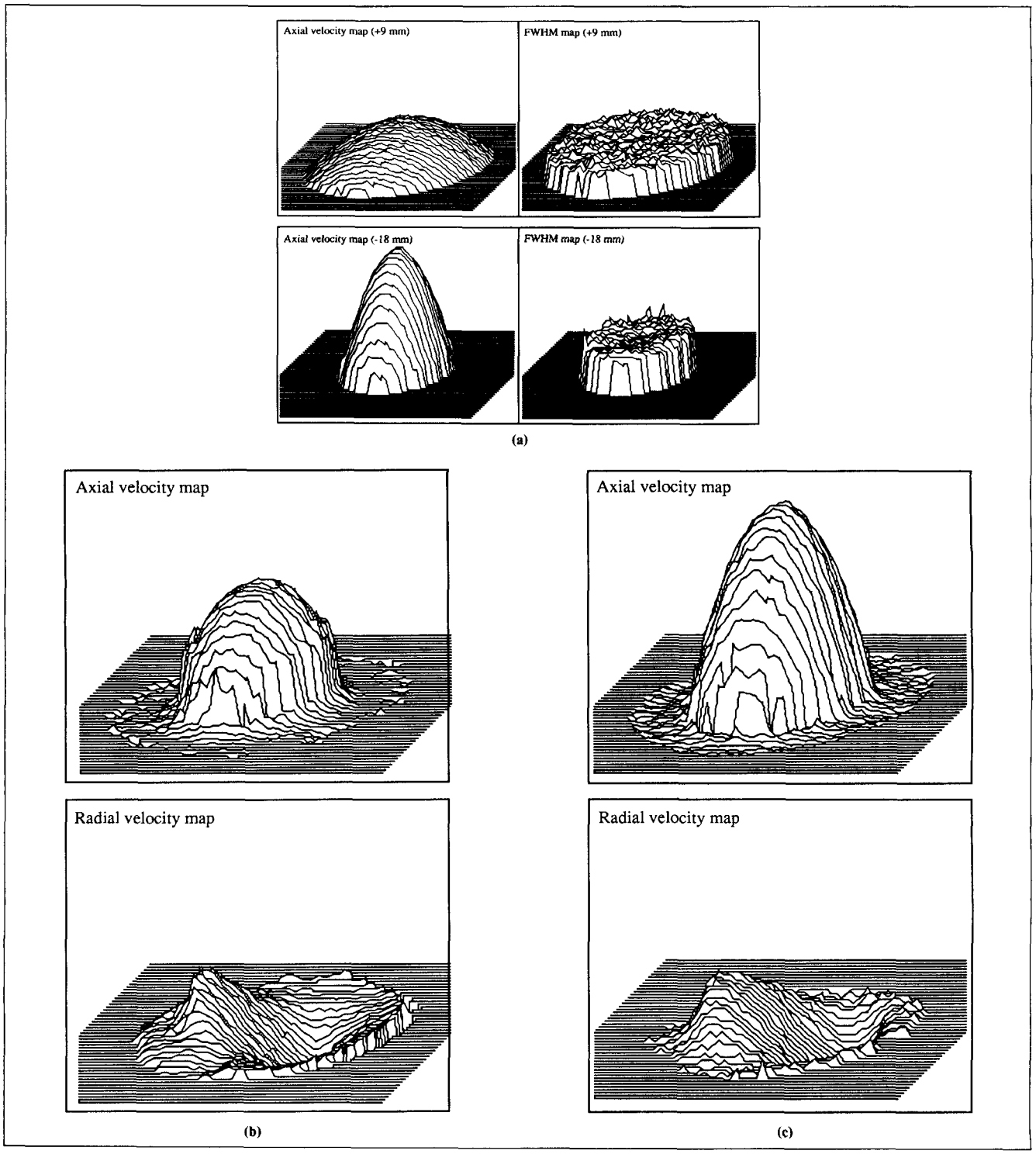

Figure 5. Velocity and diffusion maps shown as stacked plots.

The information for these maps is obtained by analyzing the dynamic displacement profiles as shown in Figure 4 for each pixel. The ordinate on the diffusion maps is the full width half maximum (FWHM) of the dynamic displacement profile and so is proportional to $D^{1/2}$. These maps agree, within experimental precision, with the value of D for free water. (a) The axial velocities and the corresponding diffusion coefficients for Poiseuille flow far from the junction regions where there is no radial velocity; (b) the radial and axial velocities at the junction for flow through a contraction; (c) the radial and axial velocities at the junction for flow through an expansion.

are parabolic and the radial velocities are zero. In the region of the junction, however, there are axial velocity profiles which are distinctly not parabolic in shape and there are measureable radial velocities. The axial velocity profiles apparent in Figure 7 in the vicinity of the expansion junction are consistent with the bell-shaped flow profiles which have been observed using high speed photography of neutrally buoyant tracer particles (Feuerstein et al., 1975).

A detailed comparison of the experimental axial and radial velocity profiles with those calculated numerical from the Na-

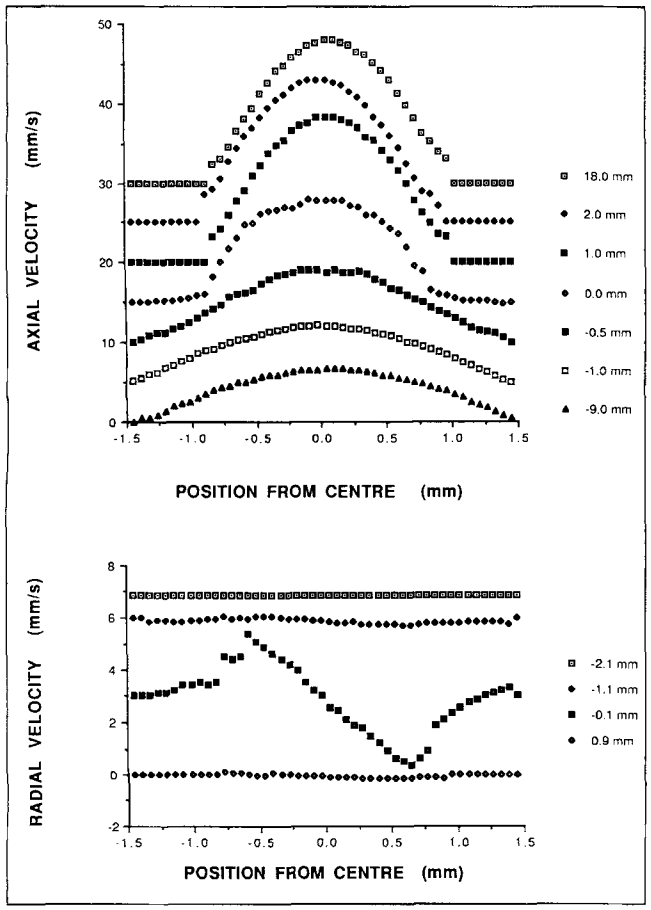

Figure 6. Axial and radial velocities for flow through an abrupt contraction.

The values are an average of the velocity within a slice perpendicular to the axis of the tube and the legend at the side of each graph indicates the center of each slice. The junction is located at 0.0 mm and negative values indicate a position to the inlet side of the junction. The slice thicknesses for the axial and radial velocities were 0.33 and 0.67 mm, respectively. Poiseuille flow is observed far from the junction region and a radial component of the velocity is observed only in the junction region. No secondary flow is observed. (Note that each velocity profile has been displaced along the ordinate axis for clarity.)

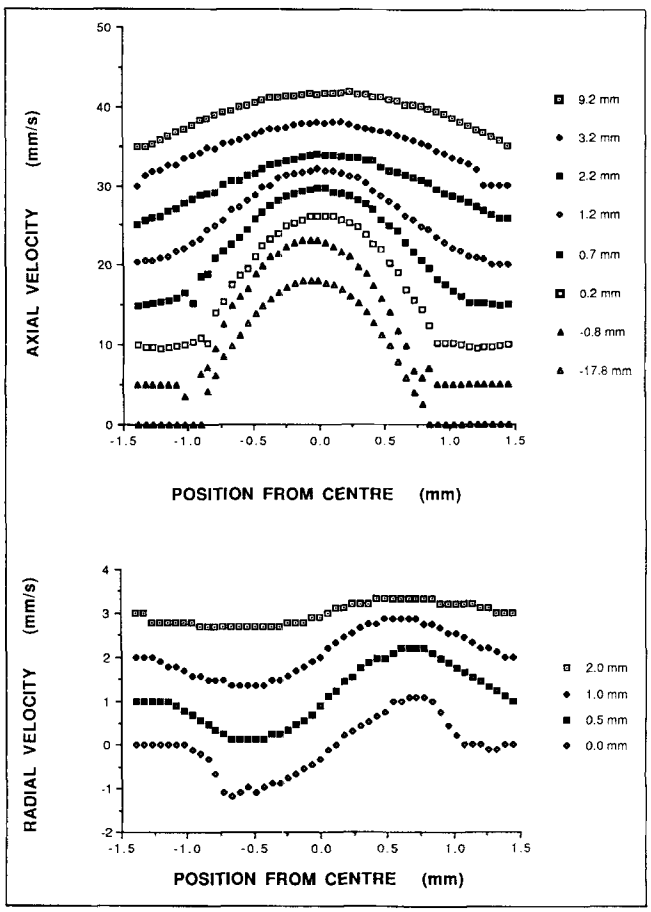

Figure 7. Axial and radial velocities for flow through an abrupt expansion.

The values are an average of the velocity within a slice perpendicular to the axis of the tube and the legend at side of each graph indicates the center of each slice. The junction is located at 0.0 mm and negative values indicate a position to the inlet side of the junction. The slice thicknesses for the axial and radial velocities were 0.33 and 0.67 mm, respectively. Poiseuille flow is observed far from the junction region and a radial component of the velocity is observed only in the junction region. Secondary flow as indicated by negative values of the axial velocity is observed for the 0.2 mm slice.

vier-Stokes equations in the junction region were carried out and are shown in Figures 8-11. Both the experimental results and the theoretical curves are scaled by the maximum velocity on the center line of the inlet tube far from the junction region. On the whole the agreement is very good considering that there are no adjustable parameters since the numerical solutions only depend on the value of the Reynolds number which can be calculated from the experimental parameters explicitly. Using the measured values of the maximum inlet velocity and the radius of the inlet tube along with the kinetic viscosity of water at 30°C, 0.804 $mm^2\ s^{-1}$, the Reynolds numbers for the contraction and expansion configuration were determined to be 12 and 20, respectively. The numerical solutions of the Navier-Stokes equations were carried out for these values of Re on a 0.05 mm square grid. The theoretical curves shown in Figures 8-11 are an average over the grid points contained within the slice thickness used experimentally; 0.33 mm for the axial velocity and 0.66 mm for the radial velocity. The positions of the slices quote on the diagrams are the positions of the centers of the slices.

Some interesting features of the flow in the junction region are immediately apparent in the profiles. For the contraction, the change from the upstream to downstream parabolic profile occurs in a very compressed region (1 mm) about the junction. The radial velocity shown in Figure 9 has dropped off from the maximum at the junction by a factor of 10 in a distance of 1 mm either upstream or downstream. From the axial velocity profiles in Figure 8 there is no clear evidence for eddies or secondary flow presumably because of the small Reynolds number for this tube configuration. Because of the method of determining the velocities on a digitized scale, small variations in axial velocity are lost on an experimental scale designed to record the large velocities on the center line, the sensitivity of the velocity scale usually being chosen so that the sampling of the maximum velocity satisfied the Nyquist theorem. To explore the junction region for the formation of secondary flow,

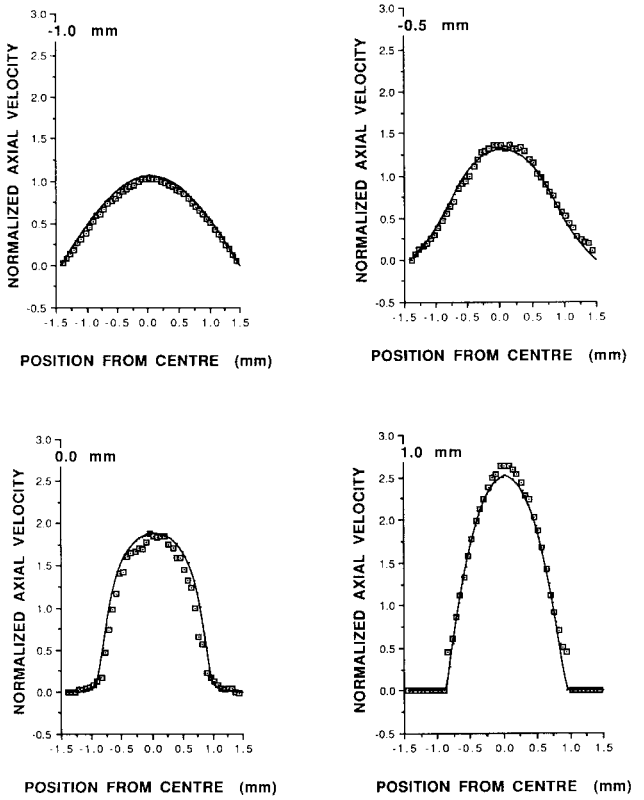

Figure 8. Comparison of the experimental and theoretical axial velocities for flow through a contraction.

Data for four positions along the stepped tube are shown.

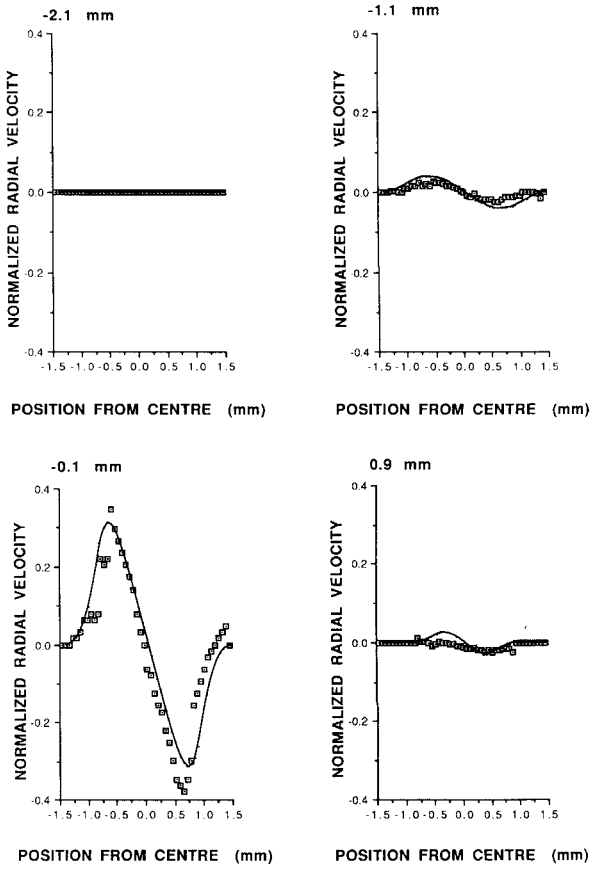

Figure 9. Comparison of the experimental and theoretical radial velocities for flow through a contraction.

Data for four positions along the stepped tube are shown. A significant radial component of the velocity is found only very near the contraction.

a more sensitive experiment was devised in which the maximum PGSE gradient was increased to 1.22 T m^{-1}. The results of this experiment were inconclusive.

In the expansion configuration measurable radial velocities and deviations from axial Poiseuille flow extend over a larger region as seen in Figure 10 and 11. At 0.2 mm the axial velocity profile in Figure 10 shows a small region of negative velocity indicative of secondary flow at the junction. It is interesting to note the changes in the radial velocity profiles shown in Figure 11 as the slice is moved progressively downstream from the junction and how well the theoretical and experimental curves agree bearing in mind the fact that the radial velocities are a factor of 10 smaller than the axial velocities.

Conclusions

This work has demonstrated that Dynamic NMR Microscopy can be used to obtain accurate measurement of the velocity vector field for nontrivial flow patterns in a reasonably short length of time. In particular, experiments were carried out to measure the axial and radial components of the velocity in the junction region of an abrupt contraction and expansion in a tube. Induced secondary flow around the abrupt junction was observed for the expansion configuration with some indication of secondary flow for the case of contraction. To our knowledge, this is the first quantitative measurement at microscopic resolution for such sample configurations. Numerical simulations were also performed on an inexpensive personal computer to predict the theoretical velocity distributions. The experimental results are in excellent agreement with the theoretical predictions.

The digital image array used in this work was constrained to 64 × 64 by the computer memory size. We have recently modified our system so that a larger digital array size can be employed in experiment, which can improve the spatial resolution of the image. Further improvement can also be made by changing the q-contrast gradient to be two-dimensional so that the axial and radial flow can be imaged at the same time, which would lead to better correlation in position between the axial and radial experiments.

While it is recognized that the imaging experiments reported here are time consuming, they contain a large amount of information not all of which is necessary for the present study of water flow under cylindrically symmetric conditions. As mentioned earlier, an experiment designed to take advantage of this symmetry could be performed in a time which is between one and two orders of magnitude shorter. Conversely it should be noted that the method used here could study asymmetric flow with no increase in the measurement time. As an example of the additional information contained in the present experiment reference is made to Figure 5 in which molecular self diffusion maps are given. While a discussion of such molecular

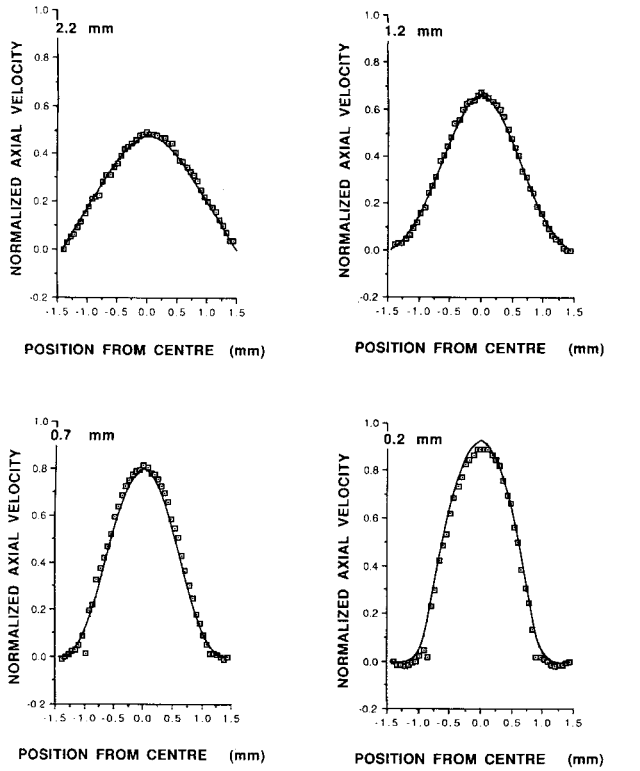

Figure 10. Comparison of the experimental and theoretical axial velocities for flow through an expansion.

Data for four positions along the stepped tube are shown. Negative values of the axial velocity are found for the slice centered at 0.2 mm indicative of secondary flow.

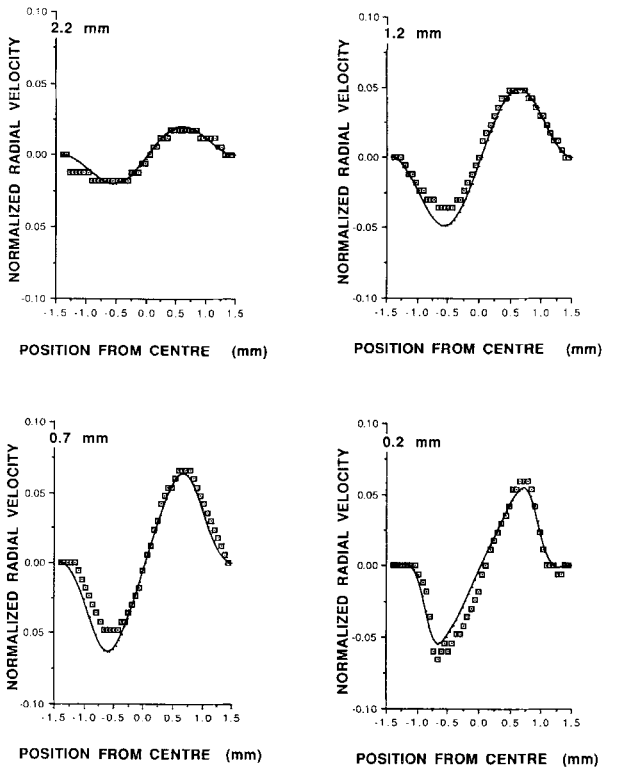

Figure 11. Comparison of the experimental and theoretical radial velocities for flow through an expansion.

Data for four positions along the stepped tube are shown.

properties is not central to this article it should be noted that they will be important to any molecular understanding of non-Newtonian flow (Xia and Callaghan, 1991).

It is expected that Dynamic NMR Microscopy measurements will have many applications in both rheology studies and hydrodynamic engineering. For example, it is now recognized that the extensional viscosity is important in any discussion of non-Newtonian fluid behavior (Barnes et al., 1989; White and Baird, 1988). Measurements of the velocity for nonviscometric flows such as those occuring at abrupt contractions and expansions are excellent tests for models of extensional flow. Velocity measurements can now easily be carried out on non-Newtonian polymer solutions using Dynamic NMR Microscopy (Xia and Callaghan, 1991). The NMR technique has excellent spatial resolution down to 10 μm. This feature should allow a very careful consideration of the behaviour of non-Newtonian fluids at solid boundaries. As pointed out by Schowalter (1988), our present knowledge of the interaction between complex fluids and surfaces is incomplete.

Literature Cited

Barnes, H. A., J. F. Hutton, and K. Walters, *An Introduction to Rheology*, Elsevier, Amsterdam (1989).

Callaghan, P. T., *Principles of Nuclear Magnetic Resonance Microscopy*, Clarendon Press, Oxford (1991).

Callaghan, P. T., C. D. Eccles, and Y. Xia, "NMR Microscopy of Dynamic Displacements: k-Space and q-Space Imaging," *J. Phys. E: Sci. Instrum.*, **21**, 820 (1988).

Callaghan, P. T., and Y. Xia, "Velocity and Diffusion Imaging in Dynamic NMR Microscopy," *J. Magn. Reson.*, **91**, 326 (1991).

Crochet, M. J., A. R. Davies, and K. Walters, *Numerical Simulation of Non-Newtonian Flow*, Elsevier Science Publishers, Amsterdam (1984).

Emrich, R. J., *Methods of Experimental Physics* Vol. 18, *Fluid Mechanics*, Academic Press, New York (1981).

Fletcher, C. A. J., *Computational Techniques for Fluid Dynamics*, Springer-Verlag, Berlin (1988).

Heath, C. A., G. Belfort, B. E. Hammer, S. D. Mirer, and J. M. Pimbley, "Magnetic Resonance Imaging and Modelling of Flow in Hollow-Fiber Bioreactors," *AIChE J.*, **36**, 547 (1990).

Jenner, C. F., Y. Xia, C. D. Eccles, and P. T. Callaghan, "Circulation of Water Within Wheat Grain Revealed by Nuclear Magnetic Resonance Micro-imaging," *Nat.*, **336**, 399 (1988).

Jensen, V. G., "Viscous Flow Around a Sphere at Low Reynolds Numbers (<40)," *Proc. Roy. Soc. London*, **A249**, 346 (1959).

Kawaguti, M., "Numerical Study of the Flow of a Viscous Fluid in a Curved Channel," *Phys. Fluid*, **II**, 101 (1969).

Köckenberger, W., Y. Xia, K. R. Jeffrey, and P. T. Callaghan, submitted to *Planta* (1992).

Latornell, D. J., and A. Pollard, "Some Observations on the Evolution of Shear Layer Instabilities in Laminar Flow through Axisymmetric Sudden Expansions," *Phys. Fluids*, **29**, 2828 (1986).

Lauterbur, P. C., "Imaging Formation by Induced Local Interactions: Examples Employing Nuclear Magnetic Resonance," *Nat.*, **242**, 190 (1973).

Macogno, E. O., and T. K. Hung, "Computational and Experimental Study of a Captive Annular Eddy," *J. Fluid Mech.*, **28**, 43 (1967).

Mansfield, P., and P. K. Grannell, "NMR 'Diffraction' in Solids," *J. Phys. C*, **6**, L422 (1973).

Moffat, H. K., "Viscous and Resistive Eddies Near a Sharp Corner," *J. Fluid Mech.*, **18**, 1 (1964).

Morris, P. G., *NMR Imaging in Biology and Medicine*, Clarendon Press, Oxford (1986).
Peyret, R., and T. D. Taylor, *Computational Methods for Fluid Flow*, Springer-Verlag, New York (1983).
Press, W. H., B. P. Flannery, S. A. Teukolsky, and W. T. Vetterling, *Numerical Recipes*, Cambridge University Press, Cambridge (1989).
Roache, P. J., *Computational Fluid Dynamics*, Hermosa Publishers, Albuquerque, New Mexico (1972).
Schowalter, W. R., "The Behaviour of Complex Fluids at Solid Boundaries," *J. Non-Newtonian Fluid Mech.*, **29**, 25 (1988).
Takemitsu, N., "Finite Difference Method to Solve Incompressible Fluid Flow," *J. Comput. Phys.*, **61**, 499 (1985).
Tanner, R. I., *Engineering Rheology*, Clarendon Press, Oxford (1985).
White, S. A., and D. G. Baird, "Flow Visualisation and Birefringence Studies on Planar Entry Flow Behaviour of Polymer Melts," *J. Non-Newtonian Fluid Mech.*, **29**, 245 (1988).
Xia, Y., and P. T. Callaghan, "A Study of Shear Thinning in High Polymer Solution Using Dynamic NMR Microscopy," *Macromol.*, **24**, 4777 (1991).

Manuscript received Aug. 6, 1991, and revision received Apr. 14, 1992.